JGR Solid Earth

RESEARCH ARTICLE
10.1029/2023JB026874

Lithospheric Evolution of the South-Central United States Constrained by Joint Inversion of Receiver Functions and Surface Wave Dispersion

Tuo Wang[1], Stephen S. Gao[2], Kelly H. Liu[2], Kevin L. Mickus[3], and Ling Chen[1]

[1]State Key Laboratory of Lithospheric Evolution, Institute of Geology and Geophysics, Chinese Academy of Sciences, Beijing, China, [2]Geology and Geophysics Program, Missouri University of Science and Technology, Rolla, MO, USA, [3]Department of Geography, Geology, and Planning, Missouri State University, Springfield, MO, USA

Key Points:

- Results provide evidence that the Sabine Block has different crustal properties from the surrounding Gulf Coastal Plain (GCP)
- Lower crustal delamination beneath the southern Ouachita Mountains is suggested by a thin and felsic crust
- Low velocities in the upper mantle of the GCP are mainly caused by the thin lithosphere and high temperatures

Supporting Information:

Supporting Information may be found in the online version of this article.

Correspondence to:

T. Wang,
twang@mail.iggcas.ac.cn

Citation:

Wang, T., Gao, S. S., Liu, K. H., Mickus, K. L., & Chen, L. (2024). Lithospheric evolution of the South-Central United States constrained by joint inversion of receiver functions and surface wave dispersion. *Journal of Geophysical Research: Solid Earth*, *129*, e2023JB026874. https://doi.org/10.1029/2023JB026874

Received 11 APR 2023
Accepted 31 MAY 2024

Author Contributions:

Conceptualization: Stephen S. Gao, Kevin L. Mickus, Ling Chen
Formal analysis: Kelly H. Liu
Investigation: Tuo Wang
Methodology: Tuo Wang
Software: Tuo Wang
Supervision: Stephen S. Gao, Ling Chen
Validation: Stephen S. Gao, Kelly H. Liu
Writing – original draft: Tuo Wang
Writing – review & editing: Tuo Wang, Stephen S. Gao, Kelly H. Liu, Kevin L. Mickus, Ling Chen

Abstract In the present study, we use broadband seismic data recorded by 190 stations of the EarthScope program's Transportable Array to construct a 3-D shear wave velocity model for the upper 180 km using a non-linear Bayesian Monte-Carlo joint inversion of receiver functions (RFs) and Rayleigh wave dispersion curves. Ambient noise and teleseismic data are used for obtaining Rayleigh wave phase velocity dispersion curves. A resonance removal filtering technique is applied to the RFs contaminated by reverberations from the thick sedimentary layers that cover most of the region. Our observations of the higher crustal shear velocities (~3.40 km/s) beneath the Sabine Block (SB), along with the estimated relatively thicker crust (~34.0 km) and lower crustal V_p/V_s estimates (~1.80) in comparison with the rest of the Gulf Coastal Plain (GCP) (~3.10 km/s for crustal shear velocities, ~29.0 km for crustal thickness, and ~1.90 for crustal V_p/V_s estimates), indicating that this crustal block has different crustal properties from the surrounding coastal plain regions. The southern Ouachita Mountains have a thin crust (~30.0 km) and low mean crustal V_p/V_s value (~1.73), suggesting that lower crustal delamination has occurred in this region. Low velocities in the upper mantle beneath most of the GCP are interpreted as a combined result of thin lithosphere, higher-than-normal temperatures, and possibly compositional variations.

Plain Language Summary The Gulf of Mexico Coastal Plain and its adjacent areas of the South-Central United States contain some of the largest hydrocarbon reserves in the world. Thus an improved understanding about the formation mechanism and evolution of the region is important for both theoretical and practical reasons. In this study, we apply several computationally intensive techniques to image the upper 180 km of the Earth's interior beneath the South-Central United States. Our results suggest that the crustal properties of the Sabine Block, located in the northern coast of the Gulf Coastal Plain (GCP), are different in comparison with the surrounding coastal plain regions. They are also consistent with the notion that the southern Ouachita Mountains have lost the lower part of its original crust into the deep mantle through a process called delamination. Low velocities are observed from approximately 30 to at least 180 km deep beneath most of the GCP, which are attributed to the thin lithosphere that allows the replacement of low-velocity asthenospheric materials, higher-than-normal temperatures of the region, and probably also compositional changes beneath the GCP.

1. Introduction

The South-Central United States (SCUS) includes a late Proterozoic rifted margin, a late Paleozoic orogenic belt that formed during the assembly of Gondwana, a late Mesozoic rifted margin that formed during the breakup of Gondwana, and a modern passive margin shelf. Imaging the lithospheric structure of the SCUS allows us to better understand the formation mechanism and evolution of the region. In spite of numerous geophysical investigations, the lithospheric structure of the SCUS remains enigmatic largely due to the presence of thick and poorly consolidated sedimentary layers within the Gulf Coastal Plain (GCP) and the late Paleozoic foreland basins (Ft. Worth and Arkoma basins [ABs]). These low-density/velocity sedimentary layers prevent reliable seismic imaging of the underlying structure and cause strong reverberations on receiver function (RF) seismograms. The reverberations mask the *P*-to-*S* converted phases from the Moho (*PmS*), which are manily used to determine the crustal thickness (H) and V_p/V_s values, leading to erroneous H and V_p/V_s determinations (Cunningham & Lekic, 2020; Langston, 2011; Zelt & Ellis, 1999). Therefore, the receiver functions (RFs) were preprocessed by adopting a resonance removal filter (Yu et al., 2015) to suppress the effect of reverberations.

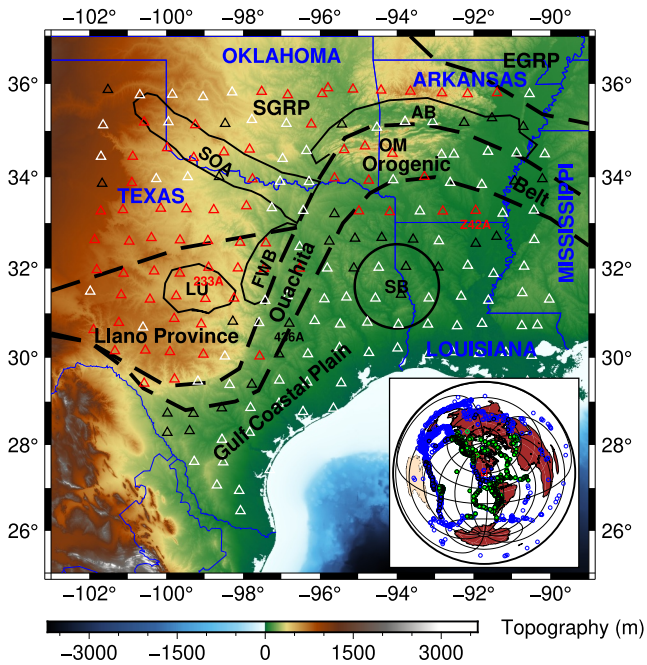

Figure 1. Map displaying seismic station locations (open triangles) and key tectonic features across the study area. State boundaries are marked by blue lines, major tectonic provinces by black dashed lines, and specific tectonic units by black solid lines. Stations are categorized and represented by red open triangles for Category A, black for Category B, and white for Category C. The inset, an azimuthal equidistant projection centered on the study area (outlined by a red rectangle), shows teleseismic events requested and utilized, with green open circles for requested events and green solid circles for utilized events in the receiver function analysis. Blue circles indicate events in the two-station analysis, with open for requested and solid for utilized. AB: Arkoma Basin; EGRP: Eastern Granite-Rhyolite Province; FWB: Ft. Worth Basin; LU: Llano Uplift; OM: Ouachita Mountains; SGRP: Southern Granite-Rhyolite Province; SB: Sabine Block; SOA: Southern Oklahoma Aulacogen.

Subsequently, the H-V_p/V_s RF stacking technique was applied to constrain the nature of the crustal structure and to generate initial velocity models and stacked RF time series for a joint inversion of RFs and surface wave dispersion curves. Surface wave dispersion curves from ambient seismic noise data were used for short periods (8–24 s) to improve the inversion resolution at shallow depths, while dispersion curves from teleseismic events were used for longer periods (32–120 s). The result is a high-resolution 3-D shear wave velocity model for the upper 180 km beneath the SCUS.

The southern portion of the study area is the GCP (Figure 1). Continental-scale RF and seismic tomography investigations have shown that the deeper structure beneath the GCP is characterized by thinner crust (~30 km) and higher V_p/V_s values (~1.83) compared to the rest of the SCUS (Ma & Lowry, 2017; Shen & Ritzwoller, 2016). However, the Sabine Block (SB) in the north central portion of the GCP has a relatively thicker crust and lower V_p/V_s values. Previous studies have proposed that the SB is possibly an oceanic island arc accreted to the North American continent as the Iapetus Ocean closed (Viele & Thomas, 1989), while others have suggested that it is a fragment of continental crust separated from North America (Lowe, 1985; Mickus & Keller, 1992) or from another continent (Viele & Thomas, 1989).

Within the GCP are the low velocities in the upper crust (Bensen et al., 2008; Gaite et al., 2012; Porter et al., 2016; Shen & Ritzwoller, 2016), which are believed to be associated with thick sedimentary layers (Laske & Masters, 1997; Mooney & Kaban, 2010; Winker & Buffler, 1988). The sedimentary layers thicken from almost zero in the Llano Uplift (LU) region to a maximum thickness of ~20 km beneath the coastline (Agrawal et al., 2015). Low velocity anomalies as low as 3% relative to the average value of the continuous U.S. are also found in the upper mantle of the GCP (Golos et al., 2020; Netto & Pulliam, 2020; Schaeffer & Lebedev, 2014; Schmandt & Lin, 2014; H. Wang, et al., 2019; Yuan et al., 2014), which may be attributed to either the high temperatures and/or compositional variations.

The Ouachita Orogenic Belt (OOB) to the north of the GCP marks the boundary between the GCP and the southern portion of the North American Craton (Figure 1). Late Paleozoic compression tectonics emplaced deep water sediments onto the North American continent and these sediments are exposed in the OM of central Arkansas and southeastern Oklahoma (Keller, Braile, et al., 1989). Mickus and Keller (1992) imaged a relatively thinner crust (~30.0 km) beneath the OM of the OOB compared to the North American Craton. As constrained by RFs, our final velocity model will aid in determining if the thinned crust exists and what is the nature of the deeper structure beneath the OM. Additionally, our crustal V_p/V_s estimates will add another constraint on physical properties in this region.

2. Geological Background

The SCUS region has experienced a series of tectonic events that spanned more than 1.7 b.y., including several complete tectonic cycles involving ocean basin closure and reopening (Mickus & Keller, 1992; Whitmeyer & Karlstrom, 2007). In the late Paleoproterozoic to Mesoproterozoic period (1.7–1.0 Ga), several island arcs were added to the proto southern North American continent forming the stable continental lithosphere (Whitmeyer & Karlstrom, 2007). During this period, the Southern and Eastern Granite-Rhyolite Provinces (1.5–1.3 Ga; Figure 1) were created by a series of silicic intrusions (Van Schmus et al., 1993). A number of orogenic thrust sheets were emplaced on the southern and eastern margins of the cratonic core of North America during the collision of Laurentia and Amazonia (Hynes & Rivers, 2010; Petersson et al., 2015), resulting in the assembly of the supercontinent Rodina (1.3–0.9 Ga; Li et al., 2008). The breakup of Rodina and the opening of the Iapetus Ocean initiated by the Neoproterozoic-Cambrian rifting in the southern United States (Cawood et al., 2001;

Hoffman, 1991; Thomas, 1991) formed several failed rifts including the Southern Oklahoma Aulacogen (SOA) (Budnik, 1986; Keller & Stephenson, 2007).

The late Paleozoic OOB, as mainly defined by a high amplitude gravity gradient (Keller, Kruger, et al., 1989), was formed along the North American continental margin. Flexure of the North American continent during the formation of the OOB created various uplifts including the LU (Mosher, 1998). Also formed were deep foreland basins including the AB in Arkansas and Oklahoma (Houseknecht, 1986) and the Ft. Worth Basin in eastern Texas (Keller, Kruger, et al., 1989). The SB to the south of the OOB was accreted to the North America during the Ouachita Orogeny (Lillie et al., 1983; Mickus & Keller, 1992). The last major tectonic event was an early Mesozoic rifting event during the initial stage of the breakup of Pangea that eventually formed the Gulf of Mexico (Mickus & Keller, 1992; Milliken & Mack, 1990). Since the final rifting event, the GCP was covered by thick Mesozoic and Cenozoic sediments, which helped form a passive continental margin.

3. Data and Methods

The broadband seismic waveforms were recorded by 190 broadband seismic stations from the Transportable Array (TA) of the EarthScope Program (Figure 1), with the majority of data recorded between 2008 and 2013. For nearby stations (stations less than one km from each other), the recorded seismic data were processed all together as if they were from one station, which yielded a total of 187 station sites. For the processing of the RFs using an H-V_p/V_s stacking analysis (Zhu & Kanamori, 2000), teleseismic events with epicentral distances between 30° and 90° were requested from the Incorporated Research Institutions for Seismology (IRIS) Data Management Center (DMC). The cutoff magnitude (M_c) for the events was constrained using $M_c = 5.2 + (\Delta_e - 30)/(90 - 30) - D_f/700$, where Δ_e is the epicentral distance in degrees, 30 and 90 are the minimum and maximum epicentral distances, D_f is the focal depth and 700 is the maximum focal depth in kilometers. The equation and the parameters used represent the optimal balance between the quantity and quality of the data (Liu & Gao, 2010). Under the M_c criteria, 1,153 events were deemed useable (Figure 1). Ambient seismic noise data used in obtaining Rayleigh wave phase velocity dispersion curves for short periods were estimated from continuous vertical-component broadband seismograms with the length of 86,400 s (i.e., 1 day). Teleseismic data used in obtaining Rayleigh wave phase velocity dispersion curves for longer periods were collected from 2,699 teleseismic events with body wave magnitude (M_b) greater than or equal to 5.7 (Figure 1). To avoid interference from the near-source effects and the higher modes of surface wave, the teleseismic events should within the epicentral distances of 10°–130°. Under the assumption that surface waves propagate along great circles, only waveforms with an angle between the back azimuth of the earthquake and the inter-station path of less than 2° were retained (H. Yao et al., 2005), and 173 teleseismic events were used (Figure 1).

To process the RFs, we first band-pass filter the three-component seismograms using a four-pole, 2-pass Bessel filter (0.06–1.2 Hz). This removes the high-frequency noise so that to enhance the signal-to-noise ratio (SNR). The SNR was defined using $\max|A_s|/|\overline{A_n}|$, where $\max|A_s|$ represents the maximum absolute value on the seismogram windowed by 8 s prior to and 12 s following the predicted first P-wave arrival time based upon the IASP91 Earth model (Kennett & Engdahl, 1991), and $|\overline{A_n}|$ represents the average absolute value on the seismogram in the time window of 5–15 s prior to the predicted arrival time (Liu & Gao, 2010). Only the seismograms with SNRs greater than or equal to 4.0 were retained (Liu & Gao, 2010; T. Wang et al., 2021). The filtered seismograms were then deconvolved from the radial component to create RFs using a frequency-domain water-level deconvolution procedure (Clayton & Wiggins, 1976).

RFs from stations located in regions covered by thick sedimentary layers may be strongly affected by reverberations within these low-density/velocity layers. To address this, a frequency-domain resonance-removal filter constructed using the amplitude (r_0) and time delay (Δt) of the first trough on the autocorrelated RFs (Yu et al., 2015) was applied to suppress these reverberations. Following this, a stacking procedure based on the approach by Zhu and Kanamori (2000) was applied to identify optimal H-V_p/V_s pairs corresponding to the maximum stacking amplitude within a search window of 20–50 km depth (with a step interval of 0.1 km) for H and 1.65 to 2.05 (with a step interval of 0.01) for V_p/V_s (Figure 2). A 10-iteration bootstrap approach (Efron & Tibshirani, 1986; Press et al., 1992) was utilized to obtain the average H and crustal V_p/V_s values beneath each station site.

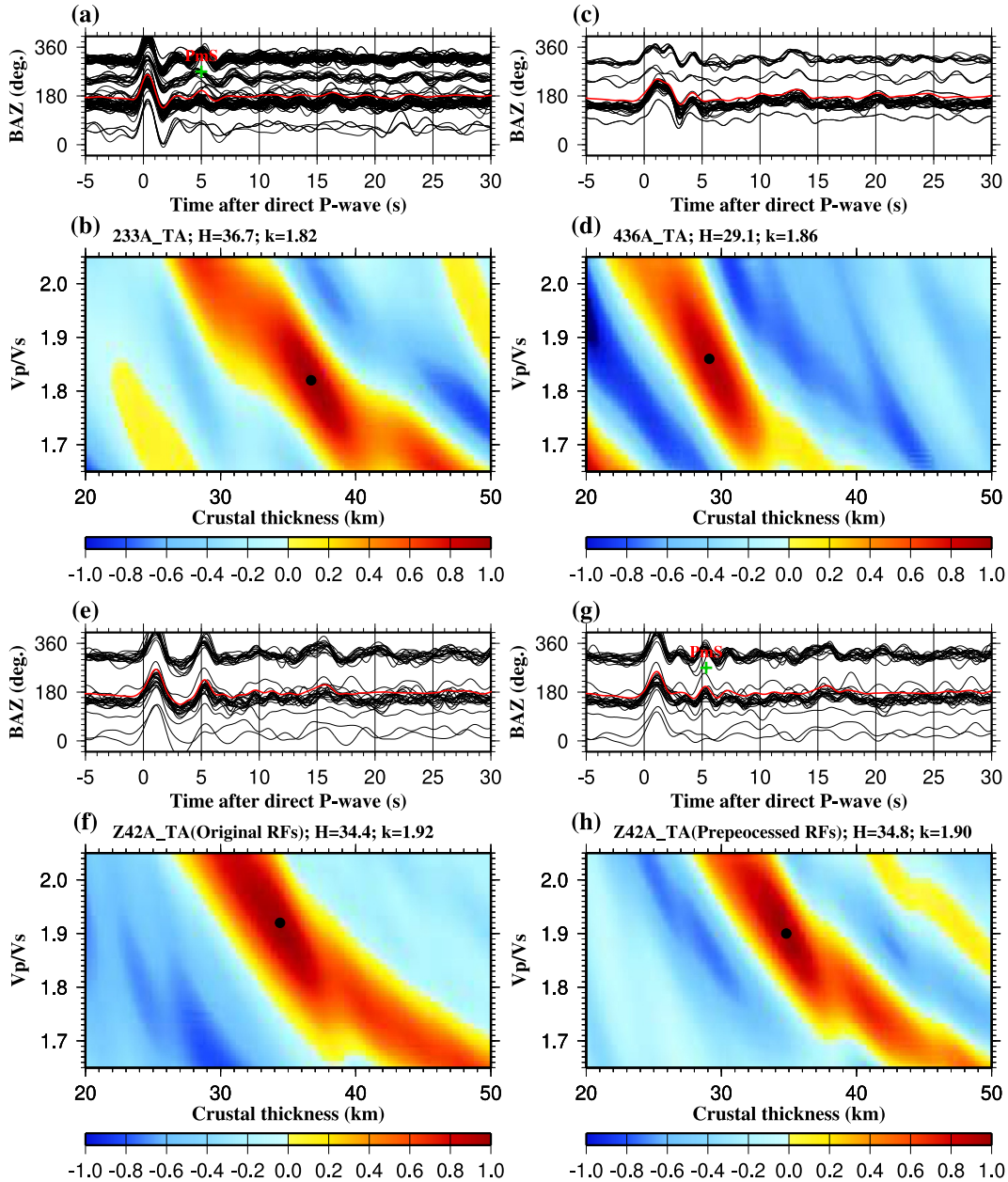

Figure 2. Receiver functions (RFs) and H-V_p/V_s analysis results. (a) Original RFs from Station 233A (Category A) showing the *P*-to-*S* converted phase (*PmS*) as a green cross and the summation trace in red. (b) H-V_p/V_s stacking amplitude map from RFs in (a), with the maximum value marked by a black dot. (c, d) Repeat of (a) and (b) for Station 436A (Category B). (e, f) Similar to (a) and (b) for Station Z42A affected by loose sediments. (g) RFs from Station Z42A after reverberation removal. (h) H-V_p/V_s stacking using RFs from (g). Station locations are shown in Figure 1.

Short-period (6–24 s with an interval of 2 s) Rayleigh wave phase velocity dispersion curves were obtained using an empirical Green's function (EGF) analysis (H. Yao et al., 2006). Seismograms recorded by each single station were processed by removing the instrument response, mean and trend. The processed seismograms were then band-pass filtered at the periods between 5 and 40 s. A temporal normalization was applied to reduce the non-stationary noise around the stations and earthquake effects (Bensen et al., 2007; H. Yao et al., 2006). Daily cross-correlations between all possible station pairs were computed to yield EGF estimates. The cross-correlations were then temporally stacked to enhance the SNR of the obtained EGF estimates. The SNR is defined by the ratio between the maximum amplitude value within a time window that contains surface wave

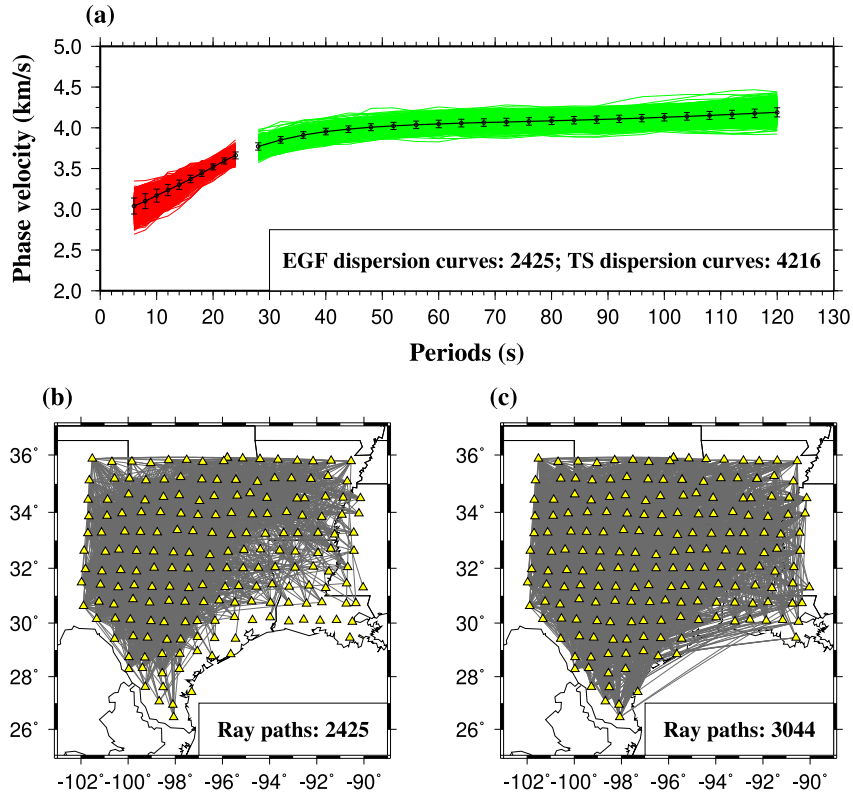

Figure 3. Dispersion curves and ray paths from the empirical Green's function (EGF) and the two-station (TS) analyses. (a) Dispersion curves with red for EGF (6–24 s) and green for TS (28–120 s). (b) EGF analysis ray paths. Yellow triangles mark the 187 station sites. (c) Ray paths for the TS analysis. Note that for one ray path, multiple estimates might be obtained, so the number of ray paths is smaller than the derived dispersion curves.

signals and the root-mean-square amplitude of the noise that follows the signal window (Bensen et al., 2007). Note that the SNR is different from the one used for constraining the RFs. Surface wave dispersion curves were calculated from the EGF estimates using a far-field representation of the surface wave Green's function and an image transformation method (H. Yao et al., 2005, 2006). An experience-based manual selection of the dispersion curves was then applied under three criteria (T. Wang, et al., 2019; H. Yao et al., 2006), which are (a) the SNR should be greater than 5; (b) the inter-station distance should be at least three wavelengths (Y. Yang et al., 2010); (c) the dispersion curves should generally agree with the global model of Shapiro and Ritzwoller (2002). Using these criteria, a total of 2,425 dispersion curves were retained (Figure 3).

Long-period (28–120 s with an interval of 4 s) dispersion curves were obtained from a teleseismic surface wave two-station (TS) analysis (H. Yao et al., 2005). Data recorded by single stations were processed by removing the instrument response and by filtering with a multiple filter technique (MFT, Dziewonski et al., 1969) to determine the group arrival times of the Rayleigh wave fundamental mode (H. Yao et al., 2005). Since the TS analysis is under the assumptions that the source and the two stations are on the same great circle path and that the two stations record a same surface wave mode, cross-correlations between the filtered seismograms of the two stations will produce relevant amplitude images (H. Yao et al., 2005). Using the image transformation method (H. Yao et al., 2005), the cross-correlation amplitude images were transformed to phase velocity images for manual selection. The same global model used for the EGF analysis (Shapiro & Ritzwoller, 2002) was applied in the selection. In total, 4,216 dispersion curves were obtained from 3,044 station pairs (Figure 3). Selected 1-D dispersion curves from both the EGF and TS analyses were inverted for 2-D phase velocity maps at different periods using the procedures of Montagner (1986) and H. Yao et al. (2010). Details of the above steps can be found in H. Yao et al. (2006) and Q. Yang et al. (2021).

To invert for a shear velocity model, phase velocities were resampled between 8 and 24 s with an interval of 4 s and between 32 and 120 s with an interval of 8 s. Given that the shortest period used was 8 s, the inverted shear

velocity model does not focus on the shallower velocity structure. Two inversion strategies, including a joint inversion of RFs and surface wave dispersion curves, and a single inversion of only the surface wave dispersion curves, were used based on the quality of the RFs. For RFs with clear *PmS* arrivals and obvious maximum stacking amplitude on the H-V_p/V_s plots (Figures 2a and 2b), the recording stations were classified as Category A. For RFs with less clear *PmS* arrivals (Figure 2c) but with H and crustal V_p/V_s estimates that could be observed on the H-V_p/V_s plots (Figure 2d), the recording stations were assigned as Category B. These H and V_p/V_s estimates were compared with the estimates from the surrounding Category A stations to improve the reliability. The joint inversion strategy was applied to the data from the stations of these two categories. Figures S1–S10 in Supporting Information S1 show five examples of Category A stations and five examples of Category B stations. A weighting factor of 0.3 was used for the RFs since the main job of the RFs (0–10 s) in the joint inversion procedure was to search for the *PmS* arrivals, and a fit to the stacked RF time series was not attempted. Stations in Category C have neither an adequate number of recorded RFs (less than 20) nor high-quality RFs that could lead to reliable H and V_p/V_s estimates. The single inversion strategy was applied to the data from stations of Category C (Figures S11–S15 in Supporting Information S1). Sixty-seven out of the 187 station sites were classified as Category A, 30 as Category B, and 90 as Category C (Figure 1).

A non-linear Bayesian Monte-Carlo algorithm was used in the inversion processes (Shen et al., 2013). This algorithm maps the data misfit across a broad range of the model space by repeatedly applying random sampling under a Bayesian frame showing a probability distribution based on the observed data. Initial inversion models were generated for the 187 sites using independently determined H and V_p/V_s parameters to reflect varying structure beneath each of these station sites. Three-layer models were constructed, with the top layer for the loose sediments, the middle layer for the crystalline crust (from the bottom of the top layer to the Moho), and the bottom layer for the uppermost mantle (from the Moho 180 km depth). The thickness of the top layers was given based on previous studies (Mooney & Kaban, 2010; Shen et al., 2013). The thickness and V_p/V_s values for the middle layers were computed using the H-V_p/V_s RF stacking approach for stations in Categories A and B. For Category C stations, the thickness values were from the CRUST1.0 model (Laske et al., 2013), and the crustal V_p/V_s values were determined according to their locations. If a station is located in the GCP or the OOB, the V_p/V_s value was set to 1.90, which is the mean value of all the V_p/V_s estimates of the stations in the two regions from Categories A and B. Similarly, the crustal V_p/V_s value for stations in the areas north of the OOB was set to 1.84. For the bottom layers, the thickness was determined by the other two layers of the initial models (180 km minus the thickness of the top and middle layers), and the V_p/V_s value was fixed to 1.75 (Shen et al., 2013). Initial shear velocities for the top layer linearly ranged between 1.5 and 2.5 km. For the middle and bottom layers, four and five cubic B-spline coefficients for shear velocities from the IASP91 model (Kennett & Engdahl, 1991) were applied, respectively. A 20% perturbation was allowed to each of the inverted shear velocities. The scaling relationship between velocities and densities (for 10 km depth) was determined by Christensen and Mooney (1995) for the crust and by Karato (1993) for the upper mantle. Q values from the PREM model (Dziewonski & Anderson, 1981) were used for a physical dispersion correction (Kanamori & Anderson, 1977). The procedures and parameters for the determination of the prior and posterior distributions closely followed the method of Shen et al. (2013), with applications for regional investigations in the continents of North America and Africa (Shen & Ritzwoller, 2016; T. Wang et al., 2022; Q. Yang et al., 2021).

4. Results

4.1. Rayleigh Wave Phase Velocities

Rayleigh wave phase velocities were inverted from the selected phase velocity dispersion curves using a grid of 0.4° × 0.4° for each period with a sampling step of 0.1°. Figure 4 shows examples of the phase velocity maps at periods of 8, 12, and 24 s from the EGF analysis, and 40, 64, and 120 s from the TS analysis. To examine the robustness of the inverted phase velocities, a standard checkerboard resolution test at all periods was performed. The synthetic target model was generated using a grid dimension of 1.5° × 1.5° (Figure S16a in Supporting Information S1), and each grid point was alternatively assigned with velocities of 3.80 or 4.20 km/s. The recovered results show that except for the southeastern portion of the study area and those along the coastline, the pattern and magnitude were well reconstructed for all periods (Figures S16b–S16g in Supporting Information S1).

Prominent low phase velocities at periods of 8 and 12 s (Figures 4a and 4b) are observed in the GCP, mainly caused by the thick sedimentary layers. Low phase velocities at these periods are also found beneath the northern

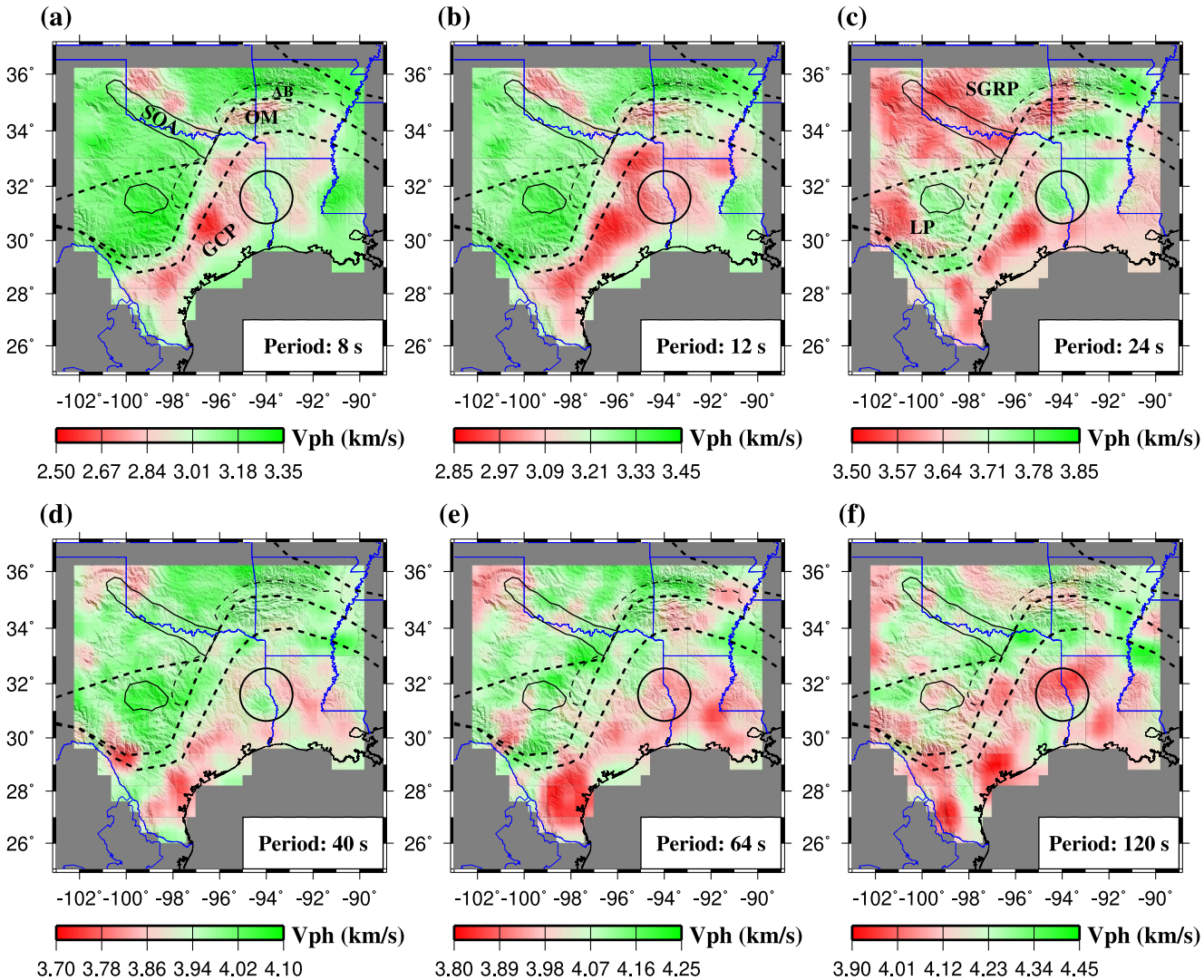

Figure 4. Phase velocity maps from the EGF and TS analyses for selected periods. EGF results for (a) 8, (b) 12, (c) 24 s; TS results for (d) 40, (e) 64, (f) 120 s. AB: Arkoma Basin; GCP: Gulf Coastal Plain; LP: Llano Province; OM: Ouachita Mountains; SGRP: Southern Granite-Rhyolite Province; SOA: Southern Oklahoma Aulacogen.

portion of the OM and a region north of the SOA. At a period of 24 s (Figure 4c), low phase velocities are found in most parts of the GCP, the Southern Granite-Rhyolite Province (SGRP), and the western part of the Llano Province (LP), while high phase velocities occur in a region south of the OM. From the periods of 40–120 s (Figures 4d–4f), the GCP is still dominated by low phase velocities, while most parts of the SGRP have high velocities.

4.2. Crustal V_p/V_s Results

The crustal V_p/V_s ratio is a parameter that can be used to estimate the bulk composition of the crust, with values lower than 1.75 suggesting an overall felsic composition, those between 1.75 and 1.81 implying an intermediate composition, and those higher than 1.81 suggesting a mafic composition (Christensen, 1996; Owens & Zandt, 1997). The mean crustal V_p/V_s value computed from the 97 seismic stations in Categories A and B (Figure 5) is 1.85 ± 0.07, suggesting an overall mafic composition of the crust (Christensen, 1996). The largest V_p/V_s value of 2.02 is observed at Station X39A in the northern OM, while the smallest V_p/V_s value of 1.72 is found at Station Y38A located in the southern Ouachita Mountains (SOM) (Figure 5b). Large V_p/V_s values are mainly found within the GCP, adjacent to the SOA, and along the OOB with the exception of the SOM (1.72 from

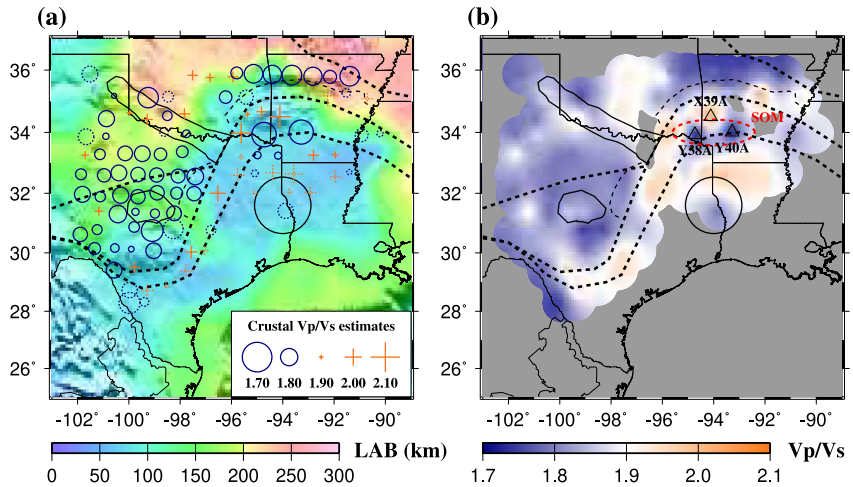

Figure 5. Crustal V_p/V_s estimates from the H-V_p/V_s approach. (a) Estimates of sparse seismic stations plotted using pluses and open circles. Solid symbols represent estimates from Category A stations, while dashed symbols are from Category B stations. The background shows the topography of the lithosphere-asthenosphere boundary (Pasyanos et al., 2014). (b) Estimates plotted by interpolating the sparse values in (a). The red dashed ellipse highlights the low V_p/V_s values observed in the southern Ouachita Mountains.

Station Y38A and 1.74 from Station Y40A; Figure 5b and Figure S17 in Supporting Information S1). Note that the V_p/V_s estimates obtained from the H-V_p/V_s analysis by filtering with the resonance removal technique do not include the loose sediments section. Given the small thickness of the loose sediments relative to that of the entire crust, the contribution of the sediments to the V_p/V_s ratios for the entire crust is expected to be small.

4.3. Crustal Thickness Results

Crustal thickness estimates were obtained from either the RF analysis (Figures 6a and 6b) or shear velocity inversion results (Figure 6c). Under the assumption that the Moho has a sharp velocity gradient (Shen et al., 2013), H values were estimated from 1-D inverted shear velocity curves by searching for the largest velocity gradient within a fixed depth window (Figure S1a in Supporting Information S1). Based on a coarse estimation from CRUST1.0 model (Laske et al., 2013), the depth window was set to 20–60 km to include all the possible Moho depths. Considering that Category C stations were not constrained by RFs during the inversion procedures, only the H estimates from stations in Categories A and B were plotted (Figure 6c). Our H estimates from the RF and shear velocity inversion analyses are quite similar (Figure 6d), and the H values discussed below are only from the shear velocity inversion results.

The mean H value for the entire study region is 39.2 ± 7.5 km with the lowest value of 24.5 km being found at Station 142A in the northern portion of the GCP and the largest value of 54.0 km being found at Station 530A in the southwestern portion of the LP (Figure 6c). Low H values mainly concentrate within the GCP and increase toward inland with a sharp H boundary along the OOB (Figure 6). Within the OOB, the SOM are characterized by relatively low H values of ~30.0 km. The mean H for the GCP is about 29.0 ± 2.2, and that for the rest of the area is 41.4 ± 6.4, leading to a crustal stretching factor (β) of 1.43.

4.4. Inverted 3-D Shear Wave Velocity Structure

Horizontal shear wave velocity depth slices (Figure 7) show similar features as those from the phase velocity maps at corresponding periods (Figure 4). Low shear wave velocities in the upper and middle crust beneath the GCP may reflect the low-density sedimentary layers (Figures 7a and 7b). At these depths, high velocity anomalies are mainly observed at the regions south of the LU and north of the AB. In the lower crust (Figure 7c), one distinct feature is the relatively higher velocities beneath the SB in comparison with the surrounding GCP areas. The uppermost mantle (Figures 7d–7f) of the GCP is characterized by relatively lower seismic velocities, compared with the rest of the study area.

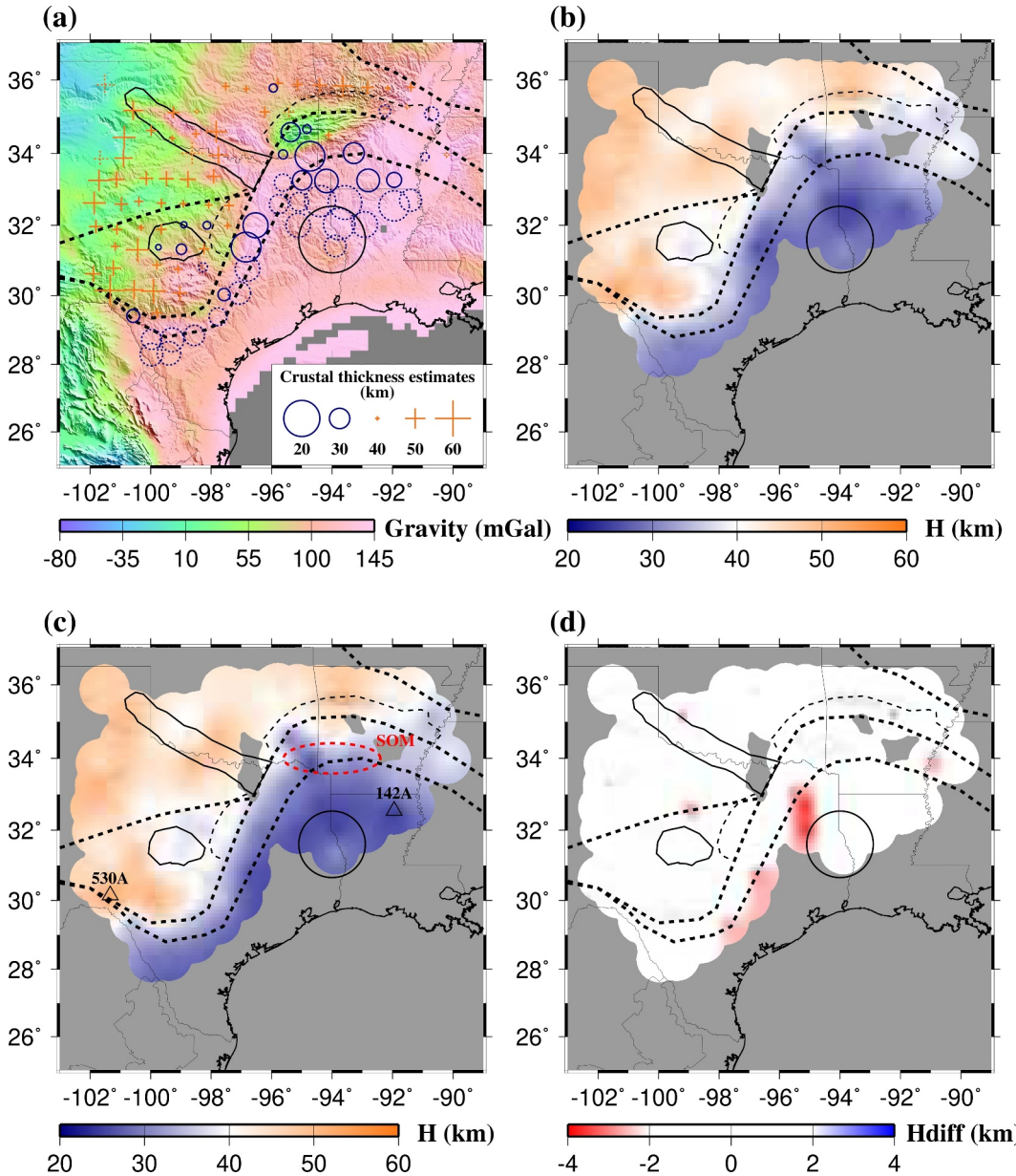

Figure 6. Crustal thickness estimates from the H-V_p/V_s and joint inversion analyses. (a) Estimates of sparse stations plotted using pluses and open circles derived from the H-V_p/V_s analysis. Solid symbols represent estimates from Category A stations, while dashed symbols from Category B stations. Background map shows Bouguer gravity field (WGM2012, Bonvalot et al., 2012). (b) Crustal thickness estimates plotted by interpolating the sparse data in (a). (c) Crustal thickness estimates obtained from the joint inversion analysis. (d) Difference between crustal thickness estimates obtained from the two analyses. SOM: southern Ouachita Mountains.

The structural features are more clearly seen in vertical cross sections (Figure 8). Profile AA' is along the NE-SW trending boundary between the GCP and the OOB, which starts from southern Texas and extends through the OM and AB (Figure 7f). The upper crust beneath the GCP is characterized by low velocities (Figure 8c). Besides the GCP, low upper crustal velocities are also found beneath the OM, which are consistent with the gravity modeling determined 14-km-thick sedimentary layer of middle to upper Paleozoic marine and nonmarine clastic sedimentary rocks (Mickus & Keller, 1992). In the lithosphere, a low velocity zone is observed beneath the GCP extending to ~180 km depth. The E-W trending Profile BB' lies over the LU, Ft. Worth Basin, OOB, and the SB in the GCP (Figure 7f). Similarly, a low velocity zone is observed in the lithosphere beneath the GCP and

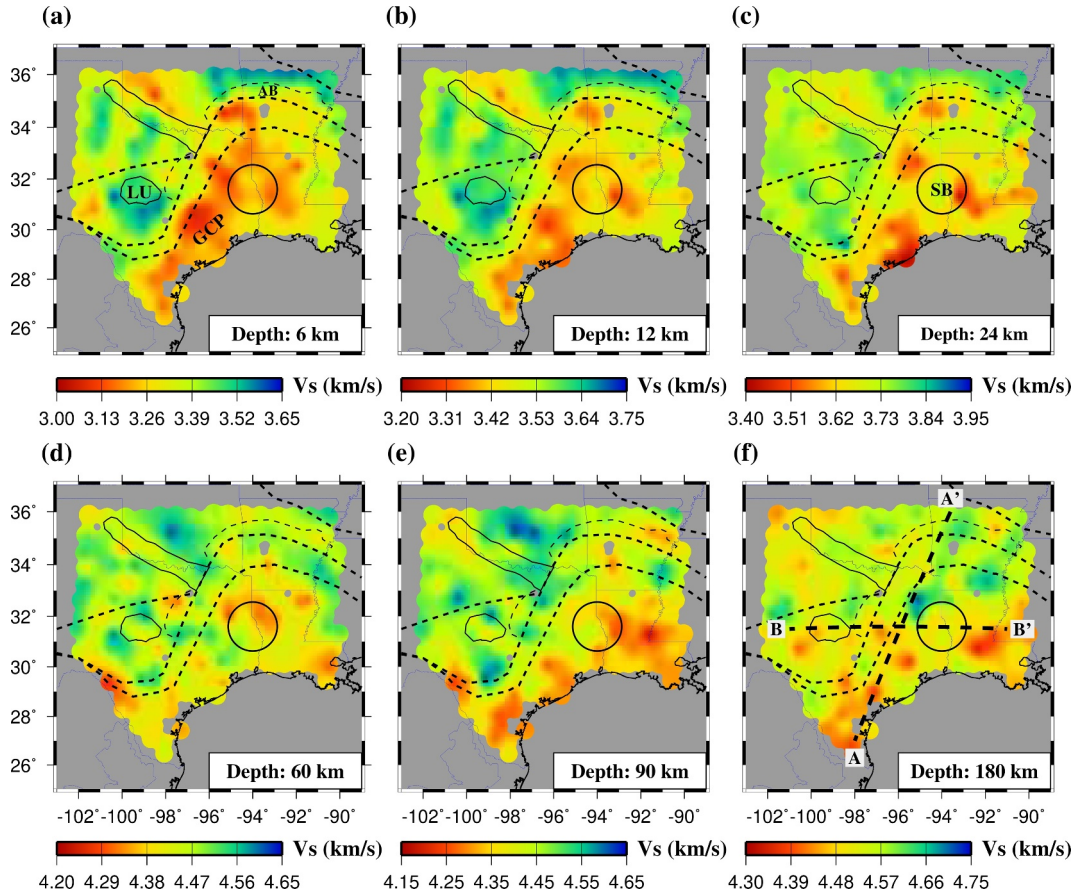

Figure 7. Shear wave velocity maps at various depths. White indicates average shear velocities from the IASP91 model at corresponding depths. Depths are shown for (a) 6, (b) 12, (c) 24, (d) 60, (e) 90, and (f) 180 km. AB: Arkoma Basin; GCP: Gulf Coastal Plain; LU: Llano Uplift; SB: Sabine Block.

diminishes toward the OOB (Figure 8f). In comparison with the surrounding GCP areas, the SB possesses a relatively faster crust (the gray dashed ellipse in Figure 8f).

5. Discussion

5.1. Comparisons With Previous Seismic Investigations

Miao et al. (2022) used an H-V_p/V_s analysis to constrain the crustal structure in the U.S. Gulf Coast. Their estimated crustal thickness ranged from 21.4 to 48.9 km, with a mean value of 35.8 km. The estimated crustal V_p/V_s ranged from 1.618 to 2.094, with a mean value of 1.857. For the 73 stations used by both studies, our mean crustal thickness value for the GCP was 37.1 ± 7.0 km and that from Miao et al. (2022) was 36.3 ± 6.1 km. The mean V_p/V_s values were 1.86 ± 0.07 from our results and 1.84 ± 0.08 from their results, respectively. A quantitative comparison of the above H and V_p/V_s estimates was conducted. The resulting cross-correlation coefficients for the H estimates was 0.96, and that for the crustal V_p/V_s estimates was 0.90 (Figure 9), implying good agreement. In the two studies, the GCP is generally characterized by a thin crust and high crustal V_p/V_s values.

Shen and Ritzwoller (2016) jointly inverted Rayleigh wave group and phase velocities, RFs, and Rayleigh wave ellipticity (H/V) estimates to construct a shear velocity model for the continuous U.S. Their Rayleigh wave phase velocity distributions are consistent with our results. At a period of 8 s, both studies found low phase velocities within the GCP, northern OM, and a region north of the SOA. The highest phase velocities (~3.35 km/s) were observed north of the AB (Figure 4a in the present study and Figure 2c in Shen & Ritzwoller, 2016). The lowest phase velocities (~3.50 km/s) for a period of 28 s were observed in the southern tip of Texas (Figure S18a in Supporting Information S1 in this study and Figure 2d in Shen & Ritzwoller, 2016). Also, the phase velocity

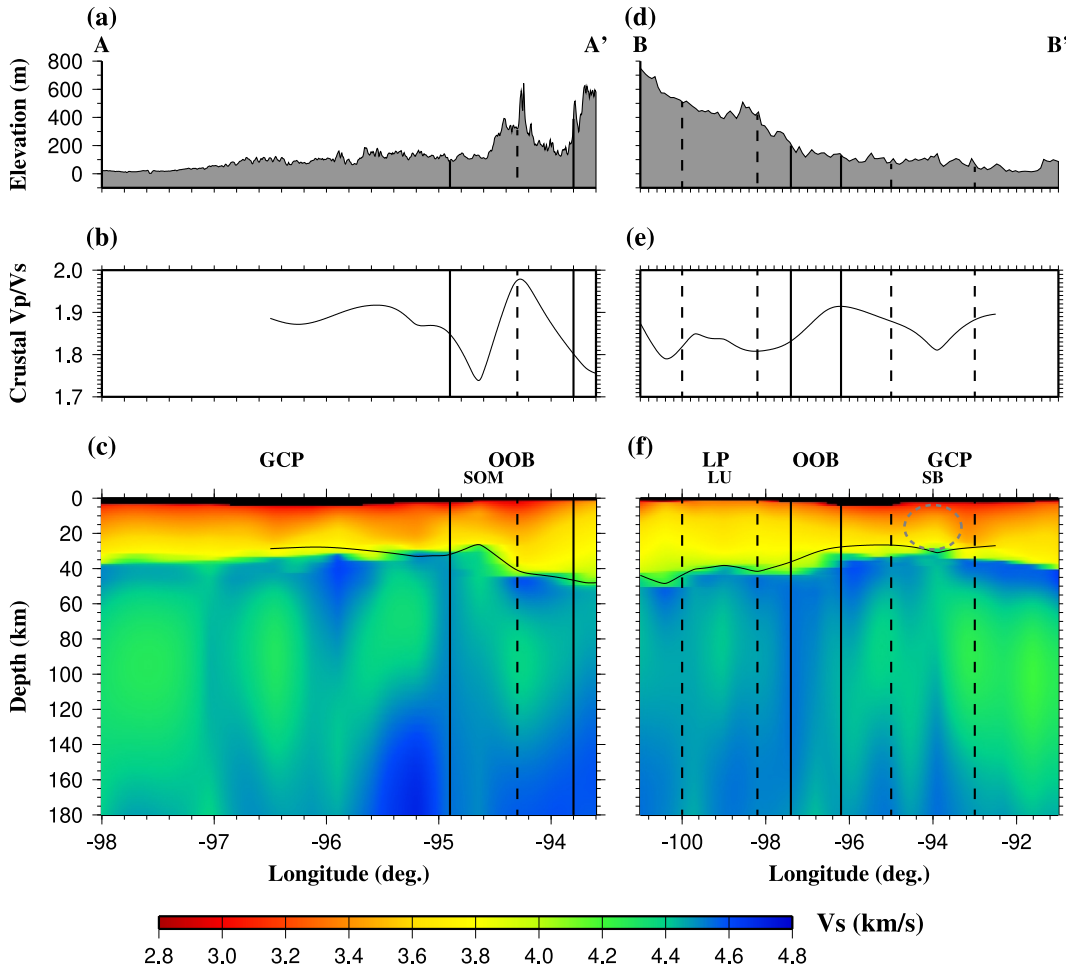

Figure 8. Profile AA' and BB' (marked in Figure 7f): (a) Elevation and (b) crustal V_p/V_s variations along Profile AA'. (c) Shear wave velocity slice to 180 km depth for AA'. Moho depths interpolated are shown as a black curve. (d)–(f) Repeat of (a)–(c) for Profile BB', with a gray dashed ellipse in (f) highlighting Sabine Block's high velocities. GCP: Gulf Coastal Plain; LP: Llano Province; LU: Llano Uplift; OOB: Ouachita Orogenic Belt; SB: Sabine Block; SOM: southern Ouachita Mountains.

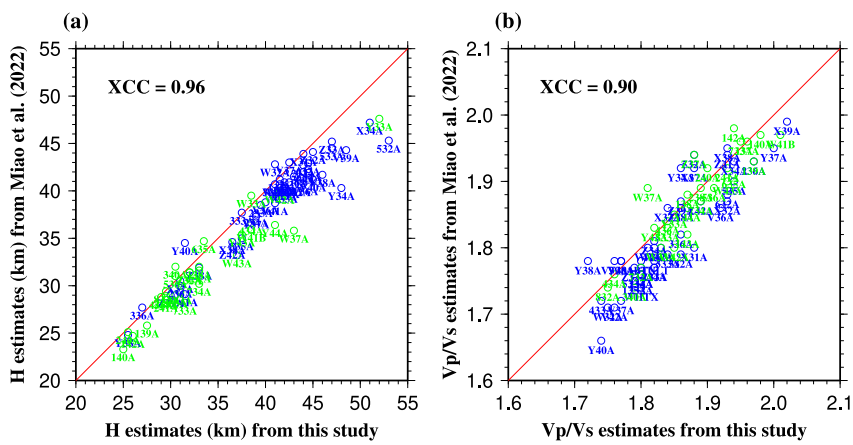

Figure 9. Comparisons of this study's H and V_p/V_s estimates with those from Miao et al. (2022) using the H-V_p/V_s method. (a) H estimates comparison. (b) V_p/V_s estimates comparison. Blue open circles represent stations from Category A, and green open circles represent stations from Category B. XCC: cross-correlation coefficient.

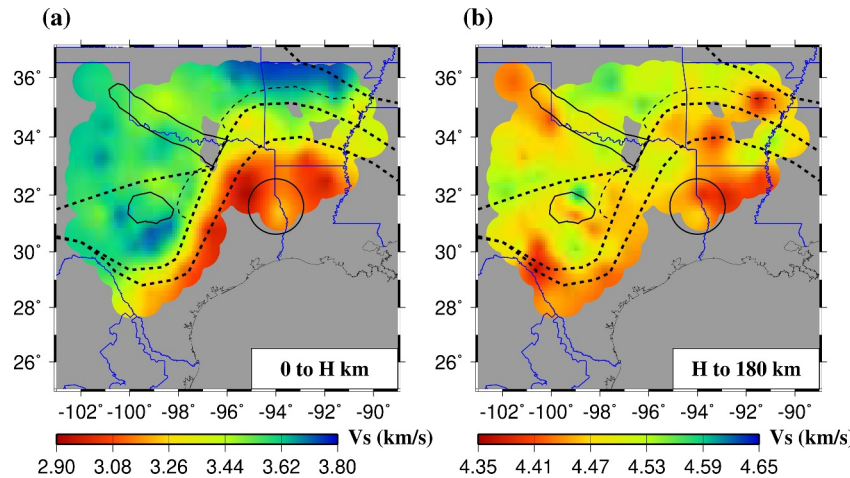

Figure 10. Mean shear wave velocity maps based on Categories A and B stations. (a) For the entire crust, and (b) for the uppermost mantle from the Moho to 180 km depth. Tectonic features are identified as in Figure 1.

values and distributions were comparable for the periods of 40 and 60 s (Figure 4d and Figure S18b in Supporting Information S1 in this study and Figures 2e and 2f in Shen & Ritzwoller, 2016).

The two studies (ours and Shen & Ritzwoller, 2016) have similar shear velocity distributions. The crust and uppermost mantle (to ∼120 km depth) beneath the GCP are characterized by low velocities (Figure 7 and Figure S19 in Supporting Information S1 in this study and Figures 12 and 18 in Shen & Ritzwoller, 2016). In general, our inverted shear velocities are lower than theirs at the same depths. At 70 km depth, our model suggests that the mean velocity values of the GCP and the rest of the study region are approximately 4.35 and 4.50 km/s, respectively (Figure S19c in Supporting Information S1). Shen and Ritzwoller (2016) found them to be about 4.50 and 4.60 km/s. Considering that the resulting velocities of the Monte-Carlo inversion are less dependent on the initial models and the similarities in phase velocities found by both studies, the most likely reason for the discrepancies could be differences in the Q parameters in the inversions.

Another discrepancy in the two shear velocity models is along the Gulf coastline, especially in the southern tip of Texas. Our velocity model indicates that low velocities are present at all depths. Meanwhile, Shen and Ritzwoller (2016) found this region to have high velocities in the lower crust and upper mantle. Since previous tomography studies have revealed either low velocities (Evanzia et al., 2014; Golos et al., 2020; Schaeffer & Lebedev, 2014; Y. Yao & Li, 2016) or high velocities (Miao et al., 2022; Porter et al., 2016), any contradictions may be due to low spatial resolution and/or poor ray-path coverage along the coastline.

5.2. Sabine Block

Our vertical velocity slice images a faster crust beneath the SB (indicated by a gray dashed ellipse in Figure 8f) compared to the surrounding areas in the GCP. This observation is corroborated by the horizontal velocity slices (Figures 7a–7c) and the mean crustal velocity map, with an average value of ∼3.40 km/s (Figure 10a). This value surpasses those of the surrounding GCP areas (∼3.10 km/s) but aligns more closely with the inland regions north of the OOB (∼3.50 km/s). The SB, situated between the Gulf Coast and the OM, remains largely enigmatic due to the absence of a detailed lithospheric structural model for the area. Mickus and Keller (1992) constructed a N-S trending gravity-based transect (presented as Figure S20b in Supporting Information S1), extending from southwestern Missouri to the Gulf of Mexico. Their gravity model indicates that the SB possesses a relatively thicker and denser crust compared to the adjacent GCP areas, suggesting that this block might be an isolated fragment (Mickus & Keller, 1992). Our observed higher crustal velocities agree with the higher crustal densities of the SB. Furthermore, our velocity model supports the hypothesis of a thicker crust (∼34.0 km) relative to the GCP areas (∼29.0 km) (Figure 6).

Moreover, our estimated crustal V_p/V_s value of ∼1.80 beneath the SB is much lower than those in the surrounding GCP areas, which generally exceed 1.90 (Figures 5 and 8e), a finding that is also reported by Miao et al. (2022). The presence of a faster crust beneath the SB, coupled with higher H and lower crustal V_p/V_s values, provide

further evidence that this block exhibits distinct crustal properties from the surrounding GCP areas. However, it remains unclear whether this crustal block separated from the North American continent (as suggested by Clift et al., 2018; Lowe, 1985; Mickus & Keller, 1992) or if it was an exotic terrane, possibly an oceanic island arc (Viele & Thomas, 1989).

5.3. Lower Crustal Delamination Beneath the Southern Ouachita Mountains

A distinct seismic velocity anomaly along the OOB is observed in the SOM, where there exists a counter-intuitive relationship between "normal" elevation and a mostly thinned crust (Figures 8a and 8c). The relatively thinner crust (~30 km), compared with the northern portion of the OM (Figure 6c), is also supported by gravity modeling (Mickus & Keller, 1992). We propose that this thin crust results from lower crustal delamination, a process that removes an eclogitized lower crust due to gravitational instability. This proposed delamination could be induced by a seaward-dipping subduction system believed to have been active within the region (Lillie et al., 1983; Mickus & Keller, 1992; Mosher, 1998; Nelson et al., 1982). Subduction systems are known to be favorable for delamination processes (Hacker et al., 2011). The compression from subduction may transform the original gabbroitic lower crust into an eclogitized lower crust through metamorphic eclogitization. This leads to densification and delamination of the crust's bottom (Bousquet et al., 1997; Rey, 1993). Such crustal thinning by delamination has been suggested in other regions along the southeastern passive continental margin, including the Carolina Terrane and Inner Piedmont of the southern Appalachian Mountains (Parker et al., 2013; Q. Yang et al., 2021).

Additional supporting evidence for the lower crustal delamination model includes the observed low mean crustal V_p/V_s value of 1.73 in the SOM (1.72 at Station Y38A and 1.74 at Station Y40A, Figure 5b and Figure S17 in Supporting Information S1). The lower crust is usually more mafic than the upper and middle crust and thus has higher V_p/V_s values. With the removal of the mafic lower crust through delamination, the mean crustal V_p/V_s values for the "remaining crust" decrease. The low crustal V_p/V_s values at Stations Y38A and Y40A are consistent with the observations by Miao et al. (2022). Additionally, our results indicate that the northern OM are characterized by an anomalously high V_p/V_s value of ~1.98, which is higher than those of the adjacent regions (Figures 5 and 8b) and the global average value of 1.78 (Christensen, 1996). The high V_p/V_s estimates in the northern OM suggest an eclogitization process prior to the delamination, given that eclogitized materials are more mafic than the original gabbro. We infer that eclogitization occurred beneath the OM, while only the southern portion has undergone sufficient change to induce delamination, considering the subduction direction is southward (Lillie et al., 1983; Nelson et al., 1982). An alternative model suggests the crust in this area was originally thin. However, this model does not account for the observed low V_p/V_s values, as a thin crust comprising upper, middle, and lower layers should maintain a normal, not lower than normal, V_p/V_s value. Furthermore, it is unlikely for an orogenic belt to feature thinner than normal crust.

5.4. Low Upper Mantle Velocities Beneath the GCP

Our shear velocity model indicates that the uppermost mantle beneath most of the GCP is characterized by lower shear wave velocities compared to the rest of the study area (Figures 7d–7f, 8c, 8f, and 10b) and the IASP91 standard Earth model. These low velocities have also been imaged by previous regional-scale (Evanzia et al., 2014; Golos et al., 2020; Netto & Pulliam, 2020; H. Wang, et al., 2019) and continental-scale (Pollitz & Mooney, 2016; Schaeffer & Lebedev, 2014; Schmandt & Lin, 2014; Shen & Ritzwoller, 2016) tomography studies. The GCP has a thin lithosphere, mainly thinner than 100 km (Figure 5a, Pasyanos et al., 2014), thus low velocities at depths greater than the lithosphere-asthenosphere boundary reflect the properties of the less dense and viscous asthenosphere. Low velocities in the lithospheric mantle (Figures 7d and 7e) are attributed to the higher-than-normal temperatures. Estimated temperature values at a depth of 100 km are approximately 1,110°C (Kaban et al., 2014; Tesauro et al., 2014), and heat flow values are about 70 mW/m^2 (Blackwell et al., 2011; Davies, 2013). The higher-than-normal temperatures are associated with the thin lithosphere of the GCP, leading to an elevated geothermal gradient. However, the highest heat flow and temperature values (Blackwell et al., 2011; Tesauro et al., 2014) do not fully correlate spatially with the lowest velocities, suggesting that other factors also contribute to the observed low velocities in the lithospheric mantle, such as a decrease in Mg # (the molar ratio 100× Mg/(Mg + Fe)) in the composition of the uppermost mantle, which lowers the velocities by increasing the proportion of the heavier Fe (Tesauro et al., 2014), or potential asthenospheric upwelling (Krauss & Menke, 2020; Y. Yao & Li, 2016).

6. Conclusions

Several conclusions can be drawn from the 3-D shear wave velocity model and the estimates of crustal thickness and V_p/V_s presented in this study: (a) The SB in the northern coast of the GCP is characterized by a thicker, faster, and less mafic crust relative to the rest GCP areas. (b) In the SOM, the thin crust and low crustal V_p/V_s values are consistent with the hypothesis of lower crustal delamination in the region. (c) Beneath most of the GCP, low shear wave velocities are observed in the upper mantle (to at least 180 km depth) and are indicative of a combination of the thinned lithosphere of the GCP, higher-than-normal temperatures, and possible compositional variations.

Data Availability Statement

All broadband seismic data used in the present study are recorded by the EarthScope program's Transportable Array (TA) (IRIS Transportable Array, 2003), and are publicly available at the Incorporated Research Institutions for Seismology Data Management Center (IRIS DMC, https://ds.iris.edu/ds/nodes/dmc). The BREQ_FAST procedure is used for requesting data with detailed information in http://ds.iris.edu/ds/nodes/dmc/forms/breqfast-request (last accessed: September 2020). Figures presented were generated using the Generic Mapping Tools (Wessel & Smith, 1995).

Acknowledgments
We would like to thank the editor, associate editor, and two reviewers for their thoughtful comments and suggestions. The facilities of IRIS Data Services, and specifically the IRIS DMC, were used for access to waveforms and related metadata used in this study. IRIS Data Services are funded through the Seismological Facilities for the Advancement of Geoscience (SAGE) Award of the National Science Foundation under Cooperative Support Agreement EAR-1851048. The study was partially supported by the U.S. National Science Foundation under awards OAC-1919789, EAR-2149587 and the American Chemical Society under award PRF-60281-ND8.

References

Agrawal, M., Pulliam, J., Sen, M. K., & Gurrola, H. (2015). Lithospheric structure of the Texas-Gulf of Mexico passive margin from surface wave dispersion and migrated Ps receiver functions. *Geochemistry, Geophysics, Geosystems*, *16*(7), 2221–2239. https://doi.org/10.1002/2015GC005803

Bensen, G. D., Ritzwoller, M. H., Barmin, M. P., Levshin, A. L., Lin, F., Moschetti, M. P., et al. (2007). Processing seismic ambient noise data to obtain reliable broad-band surface wave dispersion measurements. *Geophysical Journal International*, *169*(3), 1239–1260. https://doi.org/10.1111/j.1365-246X.2007.03374.x

Bensen, G. D., Ritzwoller, M. H., & Shapiro, N. M. (2008). Broadband ambient noise surface wave tomography across the United States. *Journal of Geophysical Research*, *113*(5), B05306. https://doi.org/10.1029/2007JB005248

Blackwell, D., Richards, M., Frone, Z., Batir, J., Ruzo, A., Dingwall, R., & Williams, M. (2011). Temperature-at-depth maps for the conterminous U.S. and geothermal resource estimates. *Transactions-Geothermal Resources Council*, *35*(2), 1545–1550.

Bonvalot, S., Balmino, G., Briais, A., Kuhn, M., Peyrefitte, A., Vales, N., et al. (2012). *World gravity map, 1: 50,000,000. Bureau Gravimetrique International (BGI)—Commission for the Geological map of the World (CGMW)*. Centre National d'Etudes Spatiales (CNES)—Institut de Recherche pour le Developpent (IRD). https://doi.org/10.18168/bgi.23

Bousquet, R., Goffe, B., Henry, P., Le Pichon, X., & Chopin, C. (1997). Kinematic, thermal and petrological model of the Central Alps: Lepontine metamorphism in the upper crust and eclogitisation of the lower crust. *Tectonophysics*, *273*(1–2), 105–127. https://doi.org/10.1016/S0040-1951(96)00290-9

Budnik, R. T. (1986). Left-lateral intraplate deformation along the ancestral rocky mountains: Implications for late Paleozoic plate motions. *Tectonophysics*, *132*(1–3), 195–214. https://doi.org/10.1016/0040-1951(86)90032-6

Cawood, P. A., McCausland, P. J. A., & Dunning, G. R. (2001). Opening Iapetus: Constraints from the Laurentian margin in Newfoundland. *Geological Society of America Bulletin*, *113*(4), 443–453. https://doi.org/10.1130/0016-7606(2001)113<0443:OICFTL>2.0.CO;2

Christensen, N. I. (1996). Poisson's ratio and crustal seismology. *Journal of Geophysical Research*, *101*(B2), 3139–3156. https://doi.org/10.1029/95JB03446

Christensen, N. I., & Mooney, W. D. (1995). Seismic velocity structure and composition of the continental crust: A global view. *Journal of Geophysical Research*, *100*(B6), 9761–9788. https://doi.org/10.1029/95JB00259

Clayton, R. W., & Wiggins, R. A. (1976). Source shape estimation and deconvolution of teleseismic bodywaves. *Geophysical Journal International*, *47*(1), 151–177. https://doi.org/10.1111/j.1365-246X.1976.tb01267.x

Clift, P. D., Heinrich, P., Dunn, D., Jacobus, A., & Blusztajn, J. (2018). The Sabine block, Gulf of Mexico: Promontory on the North American margin? *Geology*, *46*(1), 15–18. https://doi.org/10.1130/G39592.1

Cunningham, E., & Lekic, V. (2020). Constraining properties of sedimentary strata using receiver functions: An example from the Atlantic Coastal Plain of the southeastern United States. *Bulletin of the Seismological Society of America*, *110*(2), 519–533. https://doi.org/10.1785/0120190191

Davies, J. H. (2013). Global map of solid Earth surface heat flow. *Geochemistry, Geophysics, Geosystems*, *14*(10), 4608–4622. https://doi.org/10.1002/ggge.20271

Dziewonski, A. M., Bloch, S., & Landisman, M. (1969). A technique for the analysis of transient seismic signals. *Bulletin of the Seismological Society of America*, *59*(1), 427–444. https://doi.org/10.1785/bssa0590010427

Dziewonski, A. M., & Anderson, D. L. (1981). Preliminary reference Earth model. *Physics of the Earth and Planetary Interiors*, *25*(4), 297–356. https://doi.org/10.1016/0031-9201(81)90046-7

Efron, B., & Tibshirani, R. (1986). Bootstrap methods for standard errors, confidence intervals, and other measures of statistical accuracy. *Statistical Science*, *1*(1), 54–75. https://doi.org/10.1214/ss/1177013815

Evanzia, D., Pulliam, J., Ainsworth, R., Gurrola, H., & Pratt, K. (2014). Seismic Vp & Vs tomography of Texas & Oklahoma with a focus on the Gulf coast margin. *Earth and Planetary Science Letters*, *402*(C), 148–156. https://doi.org/10.1016/j.epsl.2013.12.027

Gaite, B., Iglesias, A., Villasenor, A., Herraiz, M., & Pacheco, J. F. (2012). Crustal structure of Mexico and surrounding regions from seismic ambient noise tomography. *Geophysical Journal International*, *188*(3), 1413–1424. https://doi.org/10.1111/j.1365-246X.2011.05339.x

Golos, E. M., Fang, H., & van der Hilst, R. D. (2020). Variations in seismic wave speed and Vp/Vs ratio in the North American lithosphere. *Journal of Geophysical Research: Solid Earth*, *115*(12), e2020JB020574. https://doi.org/10.1029/2020JB020574

Hacker, B. R., Kelemen, P. B., & Behn, M. D. (2011). Differentiation of the continental crust by relamination. *Earth and Planetary Science Letters*, *307*(3–4), 501–516. https://doi.org/10.1016/j.epsl.2011.05.024

Hoffman, P. F. (1991). Did the breakout of Laurentia turn Gondwanaland inside-out? *Science*, *252*(5011), 1409–1412. https://doi.org/10.1126/science.252.5011.1409

Houseknecht, D. W. (1986). Evolution from passive margin to foreland basin, the Atoka Formation of the Arkoma basin, south-central U.S.A. In P. A. Allen & P. Homewood (Eds.), *Foreland basins: International association of sedimentologists* (Vol. 8, pp. 327–345). Special Publications. https://doi.org/10.1002/9781444303810.ch18

Hynes, A., & Rivers, T. (2010). Protracted continental collision—Evidence from the Grenville Orogen. *Canadian Journal of Earth Sciences*, *47*(5), 591–620. https://doi.org/10.1139/E10-003

IRIS Transportable Array. (2003). USArray Transportable Array [Dataset]. *International Federation of Digital Seismograph Networks*. https://doi.org/10.7914/SN/TA

Kaban, M. K., Tesauro, M., Mooney, W. D., & Cloetingh, S. A. P. L. (2014). Density, temperature, and composition of the North American lithosphere-New insights from a joint analysis of seismic, gravity, and mineral physics data: 1. Density structure of the crust and upper mantle. *Geochemistry, Geophysics, Geosystems*, *15*(12), 4781–4807. https://doi.org/10.1002/2014GC005483

Kanamori, H., & Anderson, D. L. (1977). Importance of physical dispersion in surface wave and free oscillation problems: Review. *Reviews of Geophysics*, *15*(1), 105–112. https://doi.org/10.1029/RG015i001p00105

Karato, S. (1993). Importance of anelasticity in the interpretation of seismic tomography. *Geophysical Research Letters*, *20*(15), 1623–1626. https://doi.org/10.1029/93GL01767

Keller, G. R., Braile, L. W., McMechan, G. A., Thomas, W. A., Harder, S. H., Chang, W.-F., & Jardine, W. G. (1989). Paleozoic continent-ocean transition in the Ouachita Mountains imaged from PASSCAL wide-angle seismic reflection-refraction data. *Geology*, *17*(2), 119–122. https://doi.org/10.1130/0091-7613(1989)017<0119:PCOTIT>2.3.CO;2

Keller, G. R., Kruger, J., Smith, K., & Voight, W. (1989). The Ouachita system: A geophysical review. In R. Hatcher, W. Thomas, & G. Viele (Eds.), *The Appalachian-Ouachita orogen in the United States, Geological Society of America, the Geology of North America* (Vol. F-2, pp. 689–694).

Keller, G. R., & Stephenson, R. A. (2007). The Southern Oklahoma and Dniepr-Donets aulacogens: A comparative analysis. In R. Hatcher, M. Carlson, J. McBride, & C. Martinez (Eds.), *4-D Framework of continental crust: Geological Society of America Memoir 200* (pp. 127–143).

Kennett, B. L. N., & Engdahl, E. R. (1991). Traveltimes for global earthquake location and phase identification. *Geophysical Journal International*, *105*(2), 429–465. https://doi.org/10.1111/j.1365-246X.1991.tb06724.x

Krauss, Z., & Menke, W. (2020). The north Gulf anomaly: P- and S-wave travel time delays illuminate a strong thermal feature beneath the northern Gulf of Mexico. *Earth and Planetary Science Letters*, *534*(3), 116102. https://doi.org/10.1016/j.epsl.2020.116102

Langston, C. A. (2011). Wave-field continuation and decomposition for passive seismic imaging under deep unconsolidated sediments. *Bulletin of the Seismological Society of America*, *101*(5), 2176–2190. https://doi.org/10.1785/0120100299

Laske, G., & Masters, G. (1997). A global digital map of sediment thickness. *EOS Transactions American Geophysical Union*, *78*, F483.

Laske, G., Masters, G., Ma, Z., & Pasyanos, M. (2013). Update on CRUST1.0 - A 1-degree Global Model of Earth's Crust. In *Geophysical Research Abstracts, 15, Abstract EGU2013-2658*.

Li, Z. X., Bogdanova, S. V., Collins, A. S., Davidson, A., De Waele, B., Ernst, R. E., et al. (2008). Assembly, configuration, and break-up history of Rodinia: A synthesis. *Precambrian Research*, *160*(1–2), 179–210. https://doi.org/10.1016/j.precamres.2007.04.021

Lillie, R. J., Nelson, K. D., De Voogd, B., Brewer, J. A., Oliver, J. E., Brown, L. D., et al. (1983). Crustal structure of Ouachita Mountains, Arkansas; A model based on integration of COCORP reflection profiles and regional geophysical data. *American Association of Petroleum Geologists Bulletin*, *67*(6), 907–931. https://doi.org/10.1306/03b5b6cd-16d1-11d7-8645000102c1865d

Liu, K. H., & Gao, S. S. (2010). Spatial variations of crustal characteristics beneath the Hoggar swell, Algeria, revealed by systematic analyses of receiver functions from a single seismic station. *Geochemistry, Geophysics, Geosystems*, *11*(8), Q08011. https://doi.org/10.1029/2010GC003091

Lowe, D. R. (1985). Ouachita trough: Part of a Cambrian failed rift system. *Geology*, *13*(11), 790–793. https://doi.org/10.1130/0091-7613(1985)13<790:OTPOAC>2.0.CO;2

Ma, X., & Lowry, A. R. (2017). USArray imaging of continental crust in the conterminous United States. *Tectonics*, *36*(12), 2882–2902. https://doi.org/10.1002/2017TC004540

Miao, W., Niu, F., Li, G., & Levander, A. (2022). Sedimentary and crustal structure of the US Gulf Coast revealed by Rayleigh wave and teleseismic P coda data with implications for continent rifting. *Earth and Planetary Science Letters*, *577*, 117257. https://doi.org/10.1016/j.epsl.2021.117257

Mickus, K. L., & Keller, G. R. (1992). Lithospheric structure of the south-central United States. *Geology*, *20*(4), 335–338. https://doi.org/10.1130/0091-76613(1992)020<0335:LSOTSC>2.3.CO;2

Milliken, K. L., & Mack, L. E. (1990). Subsurface dissolution of heavy minerals, Frio Formation sandstones of the ancestral Rio Grande Province, South Texas. *Sedimentary Geology*, *68*(3), 187–199. https://doi.org/10.1016/0037-0738(90)90111-6

Montagner, J.-P. (1986). Regional three-dimensional structures using long period surface waves. *Annales Geophysicae*, *4*(3), 283–294.

Mooney, W. D., & Kaban, M. K. (2010). The North American upper mantle: Density, composition, and evolution. *Journal of Geophysical Research*, *115*(B12), B12424. https://doi.org/10.1029/2010JB000866

Mosher, S. (1998). Tectonic evolution of the southern Laurentian Grenville orogenic belt. *Geological Society of America Bulletin*, *110*(11), 1357–1375. https://doi.org/10.1130/0016-7606(1998)110<1357:TEOTSL>2.3.CD;2

Nelson, K. D., Lillie, R. J., de Voogd, B., Brewer, J. A., Oliver, J. E., Kaufman, S., et al. (1982). COCORP seismic reflection profiling in the Ouachita Mountains of western Arkansas: Geometry and geologic interpretation. *Tectonics*, *1*(5), 413–430. https://doi.org/10.1029/TC001i005p00413

Netto, A., & Pulliam, J. (2020). Upper mantle structure of the southern U.S. continental margin from teleseismic traveltime tomography. *Geophysical Research Letters*, *47*(7), e2019GL085482. https://doi.org/10.1029/2019GL085482

Owens, T. J., & Zandt, G. (1997). Implications of crustal property variations for model of Tibetan Plateau evolution. *Nature*, *387*(6628), 37–43. https://doi.org/10.1038/387037a0

Parker, E. H., Jr., Hawman, R. B., Fischer, K. M., & Wagner, L. S. (2013). Crustal evolution across the southern Appalachians: Initial results from the SESAME broadband array. *Geophysical Research Letters*, *40*(15), 3853–3857. https://doi.org/10.1002/grl.50761

Pasyanos, M. E., Masters, T. G., Laske, G., & Ma, Z. (2014). LITHO1.0: An updated crust and lithospheric model of the Earth. *Journal of Geophysical Research: Solid Earth*, *119*(3), 2153–2173. https://doi.org/10.1002/2013JB010626

Petersson, A., Schersten, A., Andersson, J., Whitehouse, M. J., & Baranoski, M. T. (2015). Zircon U-Pb, Hf and O isotope constraints on growth versus reworking of continental crust in the subsurface Grenville orogeny, Ohio, USA. *Precambrian Research*, *265*, 313–327. https://doi.org/10.1016/j.precamres.2015.02.016

Pollitz, F. F., & Mooney, W. D. (2016). Seismic velocity structure of the crust and shallow mantle of the Central and Eastern United States by seismic surface wave imaging. *Geophysical Research Letters*, *43*(1), 118–126. https://doi.org/10.1002/2015GL066637

Porter, R., Liu, Y., & Holt, W. E. (2016). Lithospheric records of orogeny within the continental U.S. *Geophysical Research Letters*, *43*(1), 144–153. https://doi.org/10.1002/2015GL066950

Press, W. H., Teukolsky, S. A., Vetterling, W. T., & Flannery, B. P. (1992). *Numerical recipes in FORTRAN* (2nd ed.). Cambridge University Press.

Rey, P. (1993). Seismic and tectono-metamorphic characters of the lower continental crust in Phanerozoic areas: A consequence of post-thickening extension. *Tectonics*, *12*(2), 580–590. https://doi.org/10.1029/92TC01568

Schaeffer, A. J., & Lebedev, S. (2014). Imaging the North American continent using waveform inversion of global and USArray data. *Earth and Planetary Science Letters*, *402*(C), 26–41. https://doi.org/10.1016/j.epsl.2014.05.014

Schmandt, B., & Lin, F.-C. (2014). P and S wave tomography of the mantle beneath the United States. *Geophysical Research Letters*, *41*(18), 6342–6349. https://doi.org/10.1002/2014GL061231

Shapiro, N. M., & Ritzwoller, M. H. (2002). Monte-Carlo inversion for a global shear-velocity model of the crust and upper mantle. *Geophysical Journal International*, *151*(1), 88–105. https://doi.org/10.1046/j.1365-246X.2002.01742.x

Shen, W., & Ritzwoller, M. H. (2016). Crustal and uppermost mantle structure beneath the United States. *Journal of Geophysical Research: Solid Earth*, *121*(6), 4306–4342. https://doi.org/10.1002/2016JB012887

Shen, W., Ritzwoller, M. H., Schulte-Pelkum, V., & Lin, F.-C. (2013). Joint inversion of surface wave dispersion and receiver functions: A Bayesian Monte-Carlo approach. *Geophysical Journal International*, *192*(2), 807–836. https://doi.org/10.1093/gji/ggs050

Tesauro, M., Kaban, M. K., Mooney, W. D., & Cloetingh, S. A. P. L. (2014). Density, temperature, and composition of the North American lithosphere-New insights from a joint analysis of seismic, gravity, and mineral physics data: 2. Thermal and compositional model of the upper mantle. *Geochemistry, Geophysics, Geosystems*, *15*(12), 4808–4830. https://doi.org/10.1002/2014GC005484

Thomas, W. A. (1991). The Appalachian-Ouachita rifted margin of southeastern North America. *Geological Society of American Bulletin*, *103*(3), 415–431. https://doi.org/10.1130/0016-7606(1991)103<0415:TAORMO>2.3.CO;2

Van Schmus, W. R., Bickford, M. E., Sims, P. K., Anderson, R. R., Shearer, C. K., & Treves, S. B. (1993). Proterozoic geology of the western midcontinent basement. In J. C. Reed, M. E. Bickford, R. S. Houston, P. K. Link, D. W. Rankin, P. K. Sims, et al. (Eds.), *Precambrian: Conterminous US: Boulder, Colorado, Geological Society of America, Geology of North America* (Vol. C-2, pp. 239–259).

Viele, G. W., & Thomas, W. A. (1989). Tectonic synthesis of the Ouachita orogenic belt. In R. D. Hatcher, W. A. Thomas, & G. W. Viele (Eds.), *Appalachian-Ouachita Orogen in the United States: Boulder, Colorado, Geological Society of America, Geology of North America* (Vol. F-2, pp. 695–728). https://doi.org/10.1130/DNAG-GNA-F2.695

Wang, H., Zhao, D., Huang, Z., & Wang, L. (2019). Tomography, seismotectonics, and mantle dynamics of Central and Eastern United States. *Journal of Geophysical Research: Solid Earth*, *124*(8), 8890–8907. https://doi.org/10.1029/2019JB017478

Wang, T., Feng, J., Liu, K. H., & Gao, S. S. (2019). Crustal structure beneath the Malawi and Luangwa Rift Zones and adjacent areas from ambient noise tomography. *Gondwana Research*, *67*, 187–198. https://doi.org/10.1016/j.gr.2018.10.018

Wang, T., Gao, S. S., Yang, Q., Chen, L., & Liu, K. H. (2022). Lithopheric structure underneath the Archean Tanzania Craton and adjacent regions from a joint inversion of receiver functions and Rayleigh-wave phase velocity dispersion. *Seismological Research Letters*, *93*(3), 1753–1767. https://doi.org/10.1785/0220210296

Wang, T., Gao, S. S., Yang, Q., & Liu, K. H. (2021). Crustal structure beneath the Ethiopian Plateau and adjacent areas from receiver functions: Implications for partial melting and magmatic underplating. *Tectonophysics*, *809*, 228857. https://doi.org/10.1016/j.tecto.2021.228857

Wessel, P., & Smith, W. (1995). New version of the Generic Mapping Tools released [Software]. *EOS Transactions American Geophysical Union*, *76*(29), 329. https://doi.org/10.1029/95eo00198

Whitmeyer, S. J., & Karlstrom, K. E. (2007). Tectonic model for the Proterozoic growth of North America. *Geosphere*, *3*(4), 220–259. https://doi.org/10.1130/GES00055.1

Winker, C. D., & Buffler, R. T. (1988). Paleogeographic evolution of early deep-water Gulf of Mexico and margins, Jurassic to Middle Cretaceous (Comanchean). *American Association of Petroleum Geologists Bulletin*, *72*(3), 318–346. https://doi.org/10.1306/703C8C22-1707-11D7-8645000102C1865D

Yang, Q., Liu, K. H., Wang, T., Song, J., & Gao, S. S. (2021). Crustal and upper mantle structure beneath the Southeastern United States from joint inversion of receiver functions and Rayleigh wave dispersion. *Journal of Geophysical Research: Solid Earth*, *126*(10), e2021JB021846. https://doi.org/10.1029/2021JB021846

Yang, Y., Zheng, Y., Chen, J., Zhou, S., Celyan, S., Sandvol, E., et al. (2010). Rayleigh wave phase velocity maps of Tibet and the surrounding regions from ambient seismic noise tomography. *Geochemistry, Geophysics, Geosystems*, *11*(8), Q08010. https://doi.org/10.1029/2010GC003119

Yao, H., van der Hilst, R. D., & de Hoop, M. V. (2006). Surface-wave array tomography in SE Tibet from ambient seismic noise and two-station analysis—I. Phase velocity maps. *Geophysical Journal International*, *166*(2), 732–744. https://doi.org/10.1111/j.1365-246X.2006.03028.x

Yao, H., van der Hilst, R. D., & Montagner, J.-P. (2010). Heterogeneity and anisotropy of the lithosphere of SE Tibet from surface wave array tomography. *Journal of Geophysical Research*, *115*(B12), B12307. https://doi.org/10.1029/2009JB007142

Yao, H., Xu, G., Zhu, L., & Xiao, X. (2005). Mantle structure from inter-station Rayleigh wave dispersion and its tectonic implication in western China and neighboring regions. *Physics of the Earth and Planetary Interiors*, *148*(1), 39–54. https://doi.org/10.1016/j.pepi.2004.08.006

Yao, Y., & Li, A. (2016). Lithospheric velocity model of Texas and implications for the Ouachita orogeny and the opening of the Gulf of Mexico. *Geophysical Research Letters*, *43*(23), 12046–12053. https://doi.org/10.1002/2016GL071167

Yu, Y., Song, J., Liu, K. H., & Gao, S. S. (2015). Determining crustal structure beneath seismic stations overlying a low-velocity sedimentary layer using receiver functions. *Journal of Geophysical Research: Solid Earth*, *120*(5), 3208–3218. https://doi.org/10.1002/2014JB011610

Yuan, H., French, S., Cupillard, P., & Romanowicz, B. (2014). Lithospheric expression of geological units in central and eastern North America from full waveform tomography. *Earth and Planetary Science Letters*, *402*(15), 176–186. https://doi.org/10.1016/j.epsl.2013.11.057

Zelt, B. C., & Ellis, R. M. (1999). Receiver-function studies in the Trans-Hudson orogen, Saskatchewan. *Canadian Journal of Earth Sciences*, *36*(4), 585–603. https://doi.org/10.1139/e98-109

Zhu, L., & Kanamori, H. (2000). Moho depth variation in southern California from teleseismic receiver functions. *Journal of Geophysical Research*, *105*(B2), 2969–2980. https://doi.org/10.1029/1999JB900322